

Article

# Tungsten Matrix Composite Reinforced with CoCrFeMnNi High-Entropy Alloy: Impact of Processing Routes on Microstructure and Mechanical Properties

P. V. Satyanarayana <sup>1,2</sup>, R. Sockalingam <sup>1</sup> , P. K. Jena <sup>3</sup>, K. Sivaprasad <sup>1,\*</sup> and K. G. Prashanth <sup>4,5,6,\*</sup> 

<sup>1</sup> Advanced Materials Processing Laboratory, Department of Metallurgical and Materials Engineering, National Institute of Technology, Tiruchirappalli 620015, India

<sup>2</sup> Heavy Alloy Penetrator Project (HAPP), Ordnance Factories Board, Tiruchirappalli 620025, India

<sup>3</sup> Powder Metallurgy Division, Defence Metallurgical Research Laboratory, Kanchanbagh 500058, India

<sup>4</sup> Department of Mechanical and Industrial Engineering, Tallinn University of Technology, Ehitajate tee 5, 19086 Tallinn, Estonia

<sup>5</sup> Erich Schmid Institute of Materials Science, Austrian Academy of Sciences, Jahnstraße 12, A-8700 Leoben, Austria

<sup>6</sup> CBCMT, School of Engineering, VIT University, Vellore 632014, India

\* Correspondence: ksp@nitt.edu (K.S.); kgprashanth@gmail.com (K.G.P.); Tel.: +91-944-419-2278 (K.S.); +372-5452-5540 (K.G.P.)

Received: 16 August 2019; Accepted: 7 September 2019; Published: 9 September 2019



**Abstract:** Tungsten heavy alloy composite was developed by using novel CoCrFeMnNi high-entropy alloy as the binder/reinforcement phase. Elemental tungsten (W) powder and mechanically alloyed CoCrFeMnNi high-entropy alloy were mixed gently in high energy ball mill and consolidated using different sintering process with varying heating rate (in trend of conventional sintering < microwave sintering < spark plasma sintering). Mechanically alloyed CoCrFeMnNi high-entropy alloy have shown a predominant face-centered cubic (fcc) phase with minor Cr-rich  $\sigma$ -phase. Consolidated tungsten heavy high-entropy alloys (WHHEA) composites reveal the presence of Cr–Mn-rich oxide phase in addition to W-grains and high-entropy alloys (HEA) phase. An increase in heating rate restricts the tungsten grain growth with reduces the volume fraction of the Cr–Mn-rich phase. Finally, spark plasma sintering with a higher heating rate and shorter sintering time has revealed higher compressive strength (~2041 MPa) than the other two competitors (microwave sintering: ~1962 MPa and conventional sintering: ~1758 MPa), which may be attributed to finer W-grains and reduced fraction of Cr–Mn rich oxide phase.

**Keywords:** tungsten heavy alloy; high-entropy alloy; microwave sintering; spark plasma sintering; compressive strength

## 1. Introduction

High-entropy alloys (HEA) is a novel alloying concept that got its attention since the publication of an article based on configurational entropy by Cantor et al. [1–5]. Such an alloy system shows microstructural stability at room, cryogenic, and elevated temperatures, and shows better structural properties like higher tensile/compressive strength [6–11], fracture toughness [12–14], fatigue properties [15], and creep resistance [16] and electrochemical properties (oxidation and corrosion resistance) [17–20], as the consequence of the observed simple microstructure.

The development of new alloys was restricted for past decades by the traditional alloying concept, that is, the alloying of more principal elements could lead to formation of the amorphous or complex intermetallic compounds and phases [21–24]. The introduction of the HEA concept accelerated the research in the field of materials science, where the concept of attaining simple solid solutions from multiple principal alloying elements have been established [25,26]. Yeh et al. [4] illustrated that the addition of five or more principal alloying elements, each with an atomic percentage between 5 and 35 wt % could increase the configurational entropy at a random state (larger than  $1.5R$ ). Such an increase in configurational entropy reduces the Gibb's free energy of the alloy system and forms a simple solid solution with simple fundamental crystal structures (face-centered cubic (fcc), body-centered cubic (bcc) and hexagonal closest packed (hcp) or their combination) with reduced number of phases as expected by Gibb's phase rule [3].

Researchers around the globe are extensively working on HEA research, and designing HEAs to tailor and improve the properties of the engineering materials [25–27]. One such application is the use of HEA as a reinforcement/binder in the metal matrix composites [28–30]. Tan et al. [28] has developed amorphous alloy metal matrix composite with outstanding compressive strength (~3120 MPa) by spark plasma sintering (SPS) by reinforcing Al<sub>0.6</sub>CoCrFeNi HEA particles in the Al<sub>65</sub>Cu<sub>16.5</sub>Ti<sub>18.5</sub> matrix. In another case, HEA has been used as binder for a hard tungsten-based matrix. Velo et al. [29] has developed a tungsten carbide-based cermet with a CoCrFeMnNi HEA binder. Similarly, Zhou et al. [30] has produced tungsten heavy alloy (WHA) with promising tensile strength of about 1132 MPa (~8% ductility) by using AlCrFeNiV HEA as a matrix alloy. The increase in the strength was attributable to finer W grain size and higher strength of HEA binder matrix, whereas the lower ductility was attributable to the high W–W contiguity and porosity [30].

Tungsten heavy alloys (WHA) are a two-phase metal matrix composite, where bcc structured tungsten is dispersed in the Ni-based fcc binder matrix [31–33]. The structure comprises of interconnected tungsten grains with interpenetrating matrix phase [34]. Owing to their higher density, better strength and toughness properties, they found their application in aerospace as counterbalance and in military applications such as kinetic energy penetrators [35]. These alloys are developed by sintering the powder mixture with >90 wt % of tungsten with low melting point elements such as Co, Cu, Fe, Ni, and so forth. [34–37]. Currently, WHA has been effectively produced by different processing routes like conventional liquid phase sintering, microwave sintering and spark plasma sintering [37–39]. Since the HEAs have superior mechanical properties than pure elements like Co, Cu, Fe, Ni, and so forth, and still exhibit simple fcc/bcc microstructures, there exists a novel idea of replacing the individual elements with the HEAs. This may improve the mechanical properties of the resultant composite material.

CoCrFeMnNi HEA is one of the foremost developed alloys in the HEA family introduced by Cantor [3]. Since the CoCrFeMnNi HEA shows a single fcc crystal structure [40] and contains lower melting point elements (no refractory elements), CoCrFeMnNi HEA can be used as a potential binder in the WHA system. Hence, an attempt is made to develop WHA with CoCrFeMnNi HEA binder by dispersion of 7 wt % of CoCrFeMnNi HEA prepared by mechanical alloying (MA) in 93 wt % pure tungsten by conventional, microwave and spark plasma sintering processes. The fabricated WHA with HEA binder will be mentioned as tungsten heavy high-entropy alloys (WHHEA) in upcoming discussions. This is for the first instance where WHHEA was produced by three consolidation routes and their properties were compared.

## 2. Experimental Details

### 2.1. Preparation of High-Entropy Alloy by Mechanical Alloying (MA)

The details of elemental powders used in the present study for the production of HEA is shown in Table 1. The HEA was prepared by mechanical alloying (MA) of elemental powder mixtures (Co, Cr, Fe, Mn and Ni). MA was carried out in Insmart systems Ltd., Hyderabad, India make two

station planetary ball mills. A ball-to-powder ratio of 10:1 was employed for 30 h. Wet milling was carried out with toluene as a process control agent (PCA) to avoid the oxidation and excessive welding of powder during the MA process.

**Table 1.** Details of the elemental powders used for the synthesis of single phase high-entropy alloys (HEA).

Name of the Element	Purity (%)	Avg Particle Size ( $\mu\text{m}$ )	Melting Point ( $^{\circ}\text{C}$ )	Crystal Structure	Atomic Weight
Cobalt (Co)	99.7	4	1495	hexagonal closest packed (hcp)	58.93
Chromium (Cr)	99.8	7	1907	body-centered cubic (bcc)	51.99
Iron (Fe)	99.9	4	1538	body-centered cubic (bcc)	55.85
Manganese (Mn)	99.8	7	1246	body-centered cubic (bcc)	54.94
Nickel (Ni)	99.7	4	1455	face-centered cubic (fcc)	58.69

## 2.2. Consolidation of Tungsten Heavy High-Entropy Alloy (WHHEA)

The mechanically alloyed HEA powders (7 wt %) were mixed with 93 wt % of tungsten (W) powder and subsequently ball milled gently for 24 h with a ball-to-powder ratio of 1:1. Such gentle ball milling procedure is followed to have a uniform mixture of the HEA reinforcement in the W matrix. Finally, the powders were reduced in a tubular hydrogen furnace at 600  $^{\circ}\text{C}$  for 2 h to relieve the cold working stresses that were generated during the ball milling process. Conventional sintering (CS): The reduced powders were then compacted into cylindrical bar in a cold isostatic press (Fluidhydro, Gujarat, India) at 200 MPa, followed by sintering in conventional continuous pusher type hydrogen furnace at 1450  $^{\circ}\text{C}$  for 120 min. The sintered bars were then subjected to solution annealing at 1100  $^{\circ}\text{C}$  for 4 h then oil quenched. In order to evaluate the impact of the processing routes on the microstructure and the properties, WHHEA powders were consolidated with microwave sintering (MWS) and spark plasma sintering (SPS) processes, respectively. The MWS was carried out in a 2.45 GHz furnace (Energion, New Delhi, India). The sample was placed inside a susceptor and sintering was carried out at 1450  $^{\circ}\text{C}$  for 1 h. SPS was carried out using FCT system GmbH, Frankenblick, Germany make spark plasma sintering furnace by simultaneous application of pressure and high currents using a 20 mm graphite die. A load of 50 MPa was applied at 1350  $^{\circ}\text{C}$  for 5 min during the SPS process. Temperature profiles observed in the three different processes are shown in Figure 1.

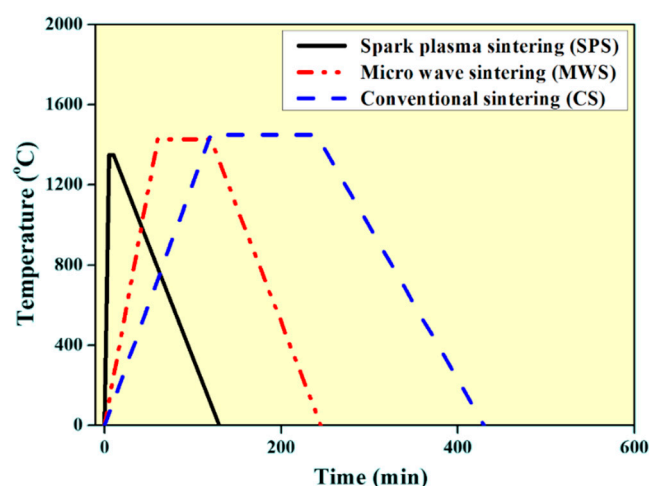


**Figure 1.** Temperature profiles observed for different processing routes (conventional sintering, microwave sintering and spark plasma sintering).

### 2.3. Characterization and Testing of Powders and Bulk Composites

The powders and consolidated bulk alloys (WHHEA) were subjected to XRD analysis (UltimaIII, Rigaku, Neu-Isenburg, Germany) for phase identification and lattice parameter calculation. The microstructure of the samples was evaluated using scanning electron microscope (SEM) (HITACHI S-3000H SEM, Mannheim, Germany). Elemental analysis was carried out using energy-dispersive X-ray spectroscopy (EDS) analyzer (Thermo scientific, Waltham, MA, USA).

The specimens with a diameter to height ratio of 1:1.1 was extracted from the consolidated WHHEAs and the compressive strength was analyzed in a universal testing machine (Asian, Ghaziabad, India) with a cross-head speed of 2 mm/min. The flexural strength was measured using the three-point bending test (Generic, Bangalore, India) with sample specification of  $1.5 \times 5 \times 40 \text{ mm}^3$  at a strain rate of 0.1/s. The hardness of the WHHEA samples were measured using Vickers microhardness tester (Ratnakar, Ichalakaranji, India). At least five readings were measured at different locations and the average values are reported.

## 3. Results and Discussion

### 3.1. Analysis of Powders

The morphology of the powders is shown in Figure 2. The SEM micrograph of the elemental W powder (Figure 2a) are cuboid in shape with an average particle size of 4  $\mu\text{m}$ . In addition, smaller satellite powder particles (1–2  $\mu\text{m}$ ) stick on the larger particles (4–8  $\mu\text{m}$ ), which may affect the flowability of the powder particles [41]. However, the presence of such satellite particle may improve the tap density of the powders, thereby adjusting between the voids during the consolidation process. The SEM micrograph of HEA powder prepared by high-energy milling is given in Figure 2b. As expected, the elemental powders lose their identity and exhibits as irregular shaped powder mixture with an average size of 2  $\mu\text{m}$ . However, the distribution of powder particle size is quite large compared to the monolithic W particles, with particles as small as 0.3  $\mu\text{m}$  and bigger particles up to ~8  $\mu\text{m}$  observed.

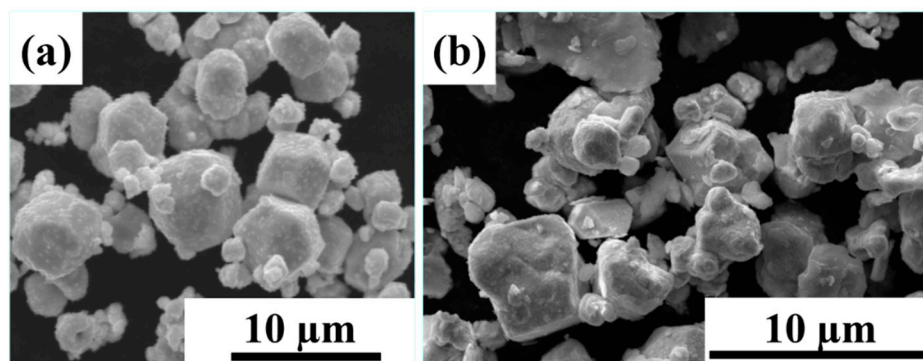


**Figure 2.** Scanning electron micrograph (SEM) images of (a) tungsten (W) particles and (b) mechanically alloyed CoCrFeMnNi HEA powder showing the powder morphology.

Figure 3 shows the X-ray diffraction patterns of elemental W powder, CoCrFeMnNi HEA powders and WHHEA bulk samples. W powders show the presence of a body-centered cubic (bcc) crystal structure, which confirms with the Joint Committee on Powder Diffraction Standards (JCPDS) number: 9-4900. On the other hand, mechanically alloyed CoCrFeMnNi HEA powders exhibit a face-centered cubic (fcc) crystal structure with minor peaks corresponding to Cr-rich  $\sigma$ -phase. Such occurrence of  $\sigma$ -phase in CoCrFeMnNi HEA was already reported by Rahul et. al. [42] during the preparation of CoCrFeMnNi HEA by mechanical alloying. Moreover, the Cr-rich  $\sigma$ -phase has been found very commonly in Cr-containing HEAs in mechanical alloyed condition [43] as well as in heat treated cast alloys [44]. However, the consolidation of such MA CoCrFeMnNi HEA by SPS was reported to promote the formation of a single phase fcc crystal structure [45], suggesting the dissolution of Cr-rich  $\sigma$ -phase

during the consolidation process. No other distinct phases other than Cr-rich  $\sigma$  phase are observed from the XRD patterns, ruling out the formation of carbides/oxides during the MA process. It may be that such compounds are present below the detectable limit of the XRD patterns. Nevertheless, with the absence of such peaks, the presence of such carbides/oxides cannot be validated.

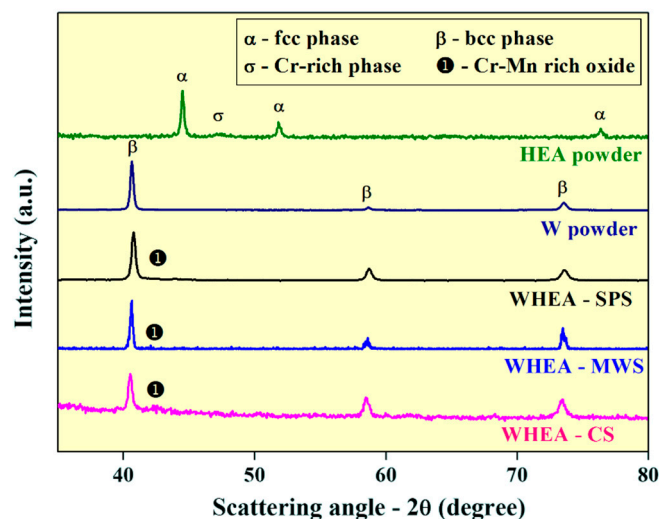


**Figure 3.** X-ray diffraction patterns of pure tungsten (W) powder, mechanically alloyed CoCrFeMnNi high-entropy alloy powder and consolidated tungsten heavy high-entropy alloys (WHHEA) samples prepared by conventional, microwave and spark plasma sintering processes.

### 3.2. Analysis of Bulk WHHEA Consolidated by Sintering

XRD patterns of bulk WHHEA composites prepared by conventional sintering (WHHEA<sub>C</sub>), microwave sintering (WHHEA<sub>M</sub>) and spark plasma sintering (WHHEA<sub>S</sub>) techniques are displayed in Figure 3. All bulk WHHEA samples predominantly show the presence of body-centered cubic (bcc) peaks that correspond to W particles with minor fraction of peaks corresponding to Cr–Mn-rich phase (PCPDF No: 89-3746). The formation of Cr–Mn-rich oxide phases was also observed after spark plasma sintering of mechanically alloyed (ethanol as PCA) CoCrFeMnNi HEA [46]. The absence of peaks corresponding to HEA (face-centered cubic phase) in the WHHEA samples suggests that the very small volume fraction of the binder phase does not fall within detectable limit of the X-ray diffractometer. Close observation on to the XRD peaks (Figure 3) of the three consolidated samples show that the intensity of the Cr–Mn-rich oxide phases increases with the decrease in the heating and cooling rates of the consolidation process. A maximum intensity is observed for the samples produced by CS and the least intensity for samples produced by SPS process, suggesting that higher exposure time and/or temperature leads to an increased formation of oxides. Hence, the time of exposure should be limited to as minimal as possible for avoiding the oxidation process. In this view, the samples produced by SPS are least exposed to high temperature and hence have the least intense Cr–Mn-rich oxide peak (minimum time available for oxidation process).

SEM images of WHHEA<sub>C</sub>, WHHEA<sub>M</sub> and WHHEA<sub>S</sub> composites are displayed in Figure 4. The microstructure of WHHEA composites is comprised of a bright tungsten particle with a greyish colored binder phase (HEA phase) [37–39]. In addition to the two phases, the microstructure also reveals a dark phase in between the HEA and W particles, as well as in between the W particles. It is in agreement with the dark Cr–Mn-rich oxide observed by Moravcik et al. in SPSed CoCrFeMnNi HEA [46]. Metallic oxide (TiO) formation was also reported in similar kinds of HEAs with substitution of titanium in place of manganese (Ni<sub>1.5</sub>Co<sub>1.5</sub>CrFeTi<sub>0.5</sub>) [47]. Hence, the WHHEA composites comprise of three phases: bright W phase, greyish HEA phase and dark Cr–Mn-rich oxide phase.

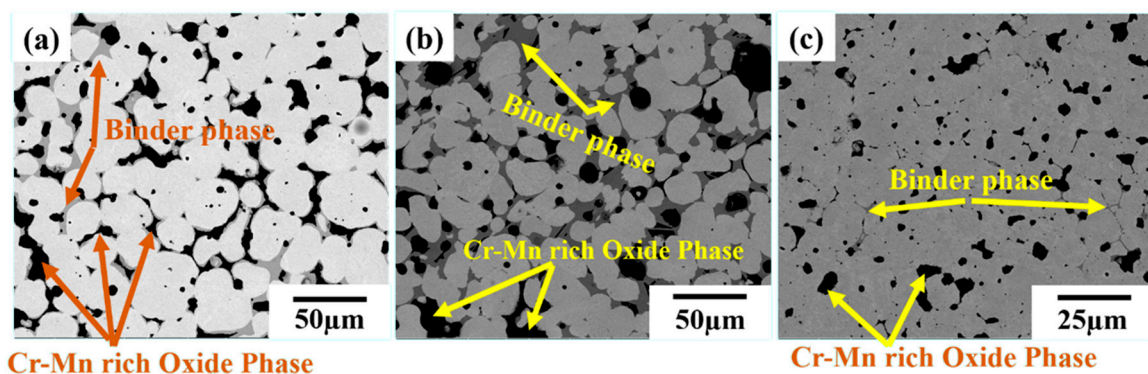


**Figure 4.** Scanning electron microscopy images of tungsten heavy high-entropy alloy (WHHEA) composites consolidated by (a) conventional sintering (CS), (b) microwave sintering (MWS) and (c) spark plasma sintering (SPS).

The elemental composition analysis results of the three different phases in WHHEA<sub>C</sub> are tabulated in Table 2. It can be noted that the greyish phase corresponds to the solid solution of CoFeNiW with minor Cr and Mn content. The bright phase corresponds to the W particles, whereas EDS analysis of the dark phases confirms that they are rich in Cr, Mn and oxygen. Such microstructural evolution can be explained thermodynamically with enthalpy of mixing between each binary pair. The mixing enthalpy of a different binary elemental pair in HEA along with tungsten particle was calculated by Miedema's approach [48,49] and given in Table 3. The positive mixing enthalpy between Cr–Mn (2.1 kJ/mol) in CoCrFeMnNi HEA enables the segregation of the compounds rich in Cr and Mn with minor other alloying elements. Such phenomenon of segregation of elements like Mn and Cr was observed during the fabrication of cemented carbides by embedding WC in CoCrFeMnNi HEA through liquid phase sintering technique [29]. The point analysis at the dark phases reveals the presence of the significant amount of tungsten (W) (Table 3). This is also due to a contribution from the higher positive enthalpy of mixing between the W–Cr (1 kJ/mol) and W–Mn (6 kJ/mol) binary pairs. Though W–Mn binary pair has a higher enthalpy of mixing (6 kJ/mol), the dark phase shows less tungsten (W) fraction than Cr and Mn; this could be due to a lower sintering temperature and the higher melting point of tungsten (W).

**Table 2.** The chemical composition of the three different phases (W, HEA and Cr–Mn-rich oxide phase) found by EDS analysis (wt %) in WHHEA composites consolidated by conventional sintering (CS).

Region Under Consideration	Co	Cr	Fe	Mn	Ni	W	O
Greyish phase	13.9	1.4	16.3	0.8	26.7	40.9	–
Bright phase	0.3	0.1	0.3	0.1	0.3	98.9	–
Dark phase	0.8	39.9	1.1	20.6	0.9	11.1	25.6

**Table 3.** Table showing the mixing enthalpy of binary pairs in WHHEA calculated by Miedema's approach [46,47].

Element	Co	Cr	Fe	Mn	Ni	W
Co	0	−4.5	−0.6	−5.2	−0.2	−1
Cr		0	−1.5	2.1	−6.7	1
Fe			0	−2.9	−1.6	0
Mn				0	−8.2	6
Ni					0	−3
W						0

EDS line mapping across the phases in WHHEA<sub>C</sub> is displayed in Figure 5. Interphase between the tungsten grain and the binder phase shows solubility of a certain fraction of tungsten in the binder

matrix. However, limited tungsten solubility in Cr–Mn-rich oxide phase, denotes the poor binding strength between the Cr–Mn oxide phase and the tungsten grain and/ binder phase.

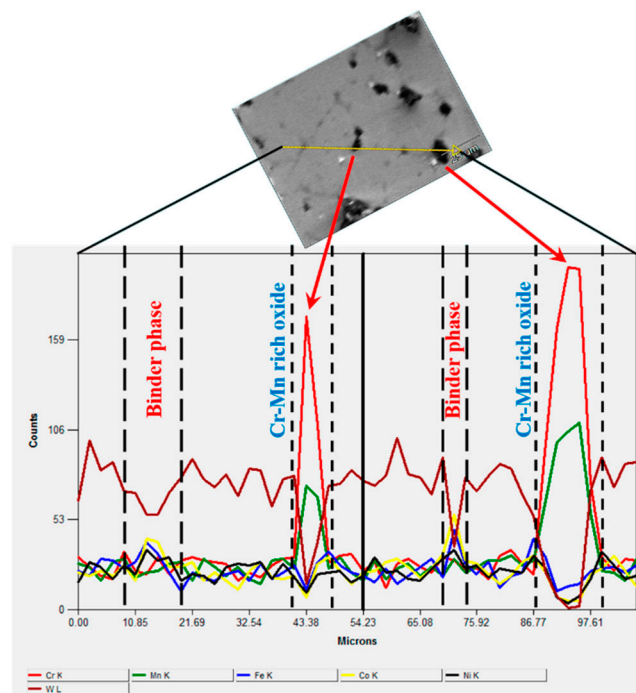


**Figure 5.** EDS line mapping across the tungsten grain, binder phase and Cr–Mn-rich oxide phase shown from the secondary image.

The average tungsten grain size and volumetric fraction of tungsten particles, HEA binder phase and Cr–Mn-rich oxide phase in WHHEA<sub>C</sub>, WHHEA<sub>M</sub> and WHHEA<sub>S</sub> are tabulated in Table 4. The variation in the tungsten grain size is attributable to heating rate, holding time and the peak temperature of the process. The sintering process with a higher heating rate, lower holding time and higher cooling rate may lead to refined tungsten grain size [50,51]. The microwave sintering with a higher heating rate (20 °C per min) than conventional sintering (5 °C per min) has shown finer tungsten grain size (33 μm). Similarly, SPS, with the highest heating rate (50 °C per min) among the three processes, has resulted in finer tungsten grain size (15 μm) due to inhibition of grain growth during fast heating, short holding. Fast heating not only refines the W-grain size, it also limits the extension of the Cr–Mn-rich oxide phase formation due to limited time availability for diffusion kinetics during the rapid heating and shorter holding time and rapid cooling. Hence, volumetric percentage of Cr–Mn-rich oxide phase is decreased with increased heating rate and shorter holding time. W-grain size and Cr–Mn-rich oxide phase fraction varies in trend of WHHEA<sub>S</sub> < WHHEA<sub>M</sub> < WHHEA<sub>C</sub>.

**Table 4.** Table showing the average W grain size and the volume fraction of the observed three different phases (W, HEA and Cr–Mn-rich oxide phase).

Consolidation Condition	W Grain Size [μm]	Average Volume Fraction of Tungsten [%]	Average Volume Fraction of HEA Phase [%]	Average Volume Fraction of Cr–Mn-Rich Oxide Phase [%]
WHHEA <sub>C</sub>	42 ± 13	74 ± 2	19 ± 2	7 ± 1
WHHEA <sub>M</sub>	33 ± 20	70 ± 2	23 ± 2	7 ± 1
WHHEA <sub>S</sub>	15 ± 7	80 ± 1	15 ± 1	5 ± 1

### 3.3. Mechanical Properties

The relative density of WHHEA<sub>S</sub>, WHHEA<sub>M</sub> and WHHEA<sub>C</sub> composites were found to be 96.3%, 96.1% and 94.8%, respectively. The density of the WHHEA is inversely proportional to the fraction of Cr–Mn-rich oxide phase. Hence, the reduction in densification may be attributed to the Cr–Mn-rich oxides formation during the consolidation process. The mechanical properties of WHHEA<sub>C</sub>, WHHEA<sub>M</sub> and WHHEA<sub>S</sub> are presented in Table 5. The micrographs of the indents are given in Figure 6. It may be observed from the size of the indents that the change in hardness are not dramatically different between the three materials considered. The Vickers hardness shows that WHHEA<sub>C</sub> exhibits comparatively higher hardness than WHHEA<sub>M</sub> and WHHEA<sub>S</sub>. However, a small increase in hardness is not accountable in determining the mechanical properties of this alloy. Compression testing was done in order to evaluate the structural properties of WHHEA composites. This is because these WHHEA composites in applications may be subjected to compressive or bending loads during metalworking or fabrication processes that involve large compressive deformation such as forging or rolling, which is required in applications such as kinetic penetrator, ballasts or pre-fragment processing of WHAs [31,32].

**Table 5.** Mechanical properties of alloy in different heating modes.

Process	Average Hardness (HV30)	Compressive Strength (MPa)	Flexural Strength (MPa)
Conventional sintering	439 ± 15	1758 ± 50	208 ± 20
Microwave sintering	431 ± 18	1962 ± 25	246 ± 15
Spark plasma sintering	422 ± 12	2041 ± 45	–

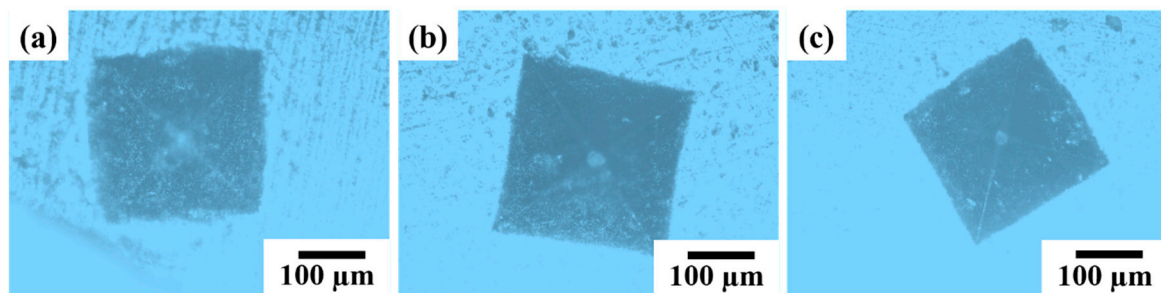


**Figure 6.** The micrograph of the indents after Vickers microhardness measurement in (a) WHHEA<sub>C</sub>, (b) WHHEA<sub>M</sub> and (c) WHHEA<sub>S</sub> respectively.

WHHEA<sub>C</sub> shows compressive strength of ~1758 MPa, whereas WHHEA<sub>M</sub> (~1962 MPa) and WHHEA<sub>S</sub> (~2041 MPa) exhibit higher compressive strengths as compared to conventional sintered parts. Moreover, the increase in strength is corroborated with tungsten (W) grain size. The WHHEA with finer W-grain size shows higher strength and confirms the application of the Hall–Petch relation in determining the strength of the alloy [52]. Figure 7 displays the graphical plot of W grain size versus compressive strength of the WHHEA composites. It clearly shows that the finer the W grain size, the higher the compressive strength is.

The three-point bend test results also show the same trend of increasing flexural strength with refinement of W grain size, where a higher flexural strength of 246 ± 15 MPa is observed for WHHEA<sub>M</sub> samples as compared to WHHEA<sub>C</sub> samples (208 ± 20 MPa). However, due to the size limitation of the samples prepared by spark plasma sintering, a three-point bending test was not carried out. Figure 8 shows the fractography of bend tested samples (WHHEA<sub>C</sub> and WHHEA<sub>M</sub>). The fracture surface reveals a brittle cleavage like feature of tungsten grains, and it may be observed that the crack initiates from the Cr–Mn-rich oxide phase. The only difference is that the WHHEA<sub>C</sub> fracture surfaces shows a number of minor cracks in tungsten grains, while the WHHEA<sub>M</sub> fracture surface does not exhibit such cracks in tungsten grains. Some ductile features may also be observed along the HEA phase, suggesting that the overall mode of failure should be a mixed mode. Ultimately, the Cr–Mn-rich oxide phase in this WHHEA alloy induces the brittleness during compressive loading and reduces the

overall strength of the WHHEA. It is in conformance with the superior strength of WHHEA<sub>5</sub> with a lower fraction of Cr–Mn-rich oxide phase among them.

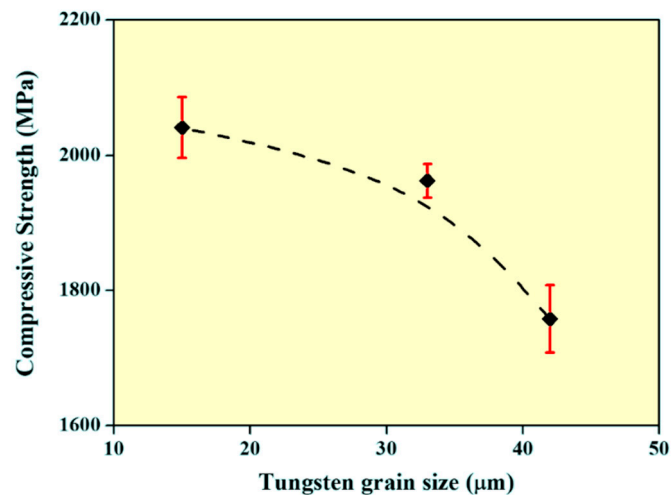


**Figure 7.** Variation of compressive strength with W grain size (as a function of different sintering processes).

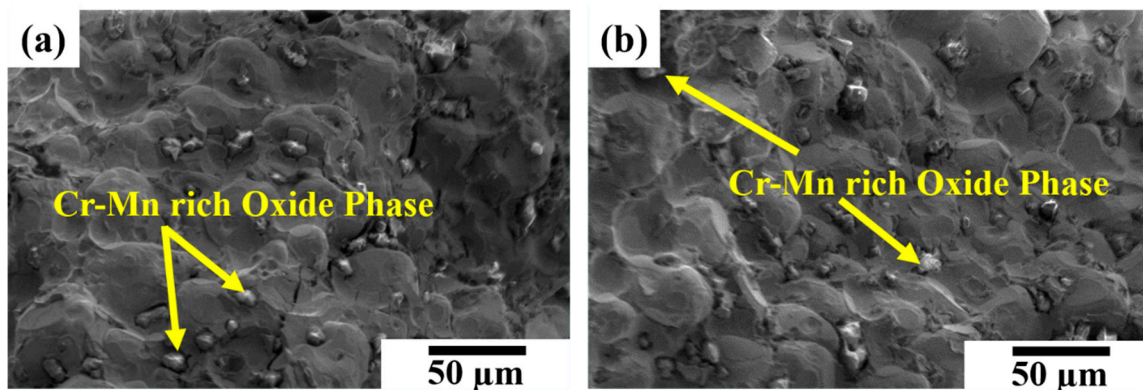


**Figure 8.** Fractography of bend tested WHHEA specimen consolidated using (a) conventional and (b) microwave sintering process.

#### 4. Conclusions

In the present study a tungsten heavy alloy has been successfully processed with CoCrFeMnNi high-entropy alloy as binder/reinforcement by conventional, microwave and spark plasma sintering techniques. The structure property correlation for WHHEA composites prepared by different sintering techniques with different heating rates/modes was also carried out and the summary of the present work is as follows:

- (1) High-energy mechanical alloying of the elemental powders in equimolar proportion result in the formation of CoCrFeMnNi high-entropy alloy with predominant fcc phase and minor  $\sigma$ -phase.
- (2) Tungsten heavy alloy (WHA) can be prepared with CoCrFeMnNi high-entropy alloy as binder/reinforcement without any crack formation by conventional, microwave and spark plasma sintering techniques.
- (3) High heating rate and shorter holding time in sintering have resulted in significant reduction of W grain size and reduced volume fraction of Cr–Mn-rich oxide phase in WHHEA.
- (4) Compressive strength and bending strength of WHHEA is more when sintering techniques with a higher heating rate and shorter holding time are employed, due to finer W grain size (microstructures).

**Author Contributions:** Conceptualization, K.S. and K.G.P.; methodology, K.S.; experiments, P.V.S., R.S., and P.K.J.; formal analysis, P.V.S., and R.S.; investigation, P.V.S., R.S., K.S. and K.G.P.; writing—original draft preparation, P.V.S. and R.S.; writing—review and editing, P.V.S., R.S., K.S., and K.G.P.; supervision, K.S. and K.G.P.

**Funding:** K.G. Prashanth acknowledges the support from the Estonian Research Council through the MOBERC15 project.

**Acknowledgments:** R. Sokkalingam acknowledges DoRA fellowship for supporting his stay at Tallinn University of Technology, Estonia.

**Conflicts of Interest:** The authors declare no conflict of interest.

## References

1. Zhang, Y.; Zuo, T.; Tang, Z.; Gao, M.C.; Dahmen, K.A.; Liaw, P.K.; Lu, Z.P. Microstructures and properties of high-entropy alloys. *Prog. Mater. Sci.* **2014**, *61*, 1–93. [[CrossRef](#)]
2. Ye, Y.F.; Wang, Q.; Lu, J.; Liu, C.T.; Yang, Y. High-entropy alloy: Challenges and prospects. *Materialstoday* **2016**, *19*, 349–362. [[CrossRef](#)]
3. Cantor, B.; Chang, I.T.H.; Knight, P.; Vincent, A.J.B. Microstructural development in equiatomic multicomponent alloys. *Mater. Sci. Eng. A* **2004**, *213*, 375–377. [[CrossRef](#)]
4. Yeh, J.W.; Chen, S.K.; Lin, S.J.; Gan, J.Y.; Chin, T.S.; Shun, T.T.; Tsau, C.H.; Chang, S.Y. Nanostructured High-Entropy Alloys with Multiple Principal Elements: Novel Alloy Design Concepts and Outcomes. *Adv. Eng. Mater.* **2004**, *6*, 299–303. [[CrossRef](#)]
5. Maity, T.; Prashanth, K.G.; Balci, O.; Kim, J.T.; Schoeberl, T.; Wang, Z.; Eckert, J. Influence of severe straining and strain rate on the evolution of dislocation structures during micro-/nanoindentation in high entropy eutectics. *Int. J. Plast.* **2018**, *109*, 121–136. [[CrossRef](#)]
6. Lv, Y.; Hu, R.; Yao, Z.; Chen, J.; Xu, D.; Liu, Y.; Fan, X. Cooling rate effect on microstructure and mechanical properties of Al<sub>x</sub>CoCrFeNi high entropy alloys. *Mater. Des.* **2017**, *132*, 392–399. [[CrossRef](#)]
7. Wang, F.J.; Zhang, Y.; Chen, G.L.; Davies, H.A. Tensile and compressive mechanical behavior of a CoCrCuFeNiAl<sub>0.5</sub> high entropy alloy. *Int. J. Mod. Phys. B* **2009**, *23*, 1254–1259. [[CrossRef](#)]
8. Sokkalingam, R.; Mishra, S.; Cheethirala, S.R.; Muthupandi, V.; Sivaprasad, K. Enhanced Relative Slip Distance in Gas-Tungsten-Arc-Welded Al<sub>0.5</sub>CoCrFeNi High-Entropy Alloy. *Metall. Mater. Trans. A* **2017**, *48*, 3630–3634. [[CrossRef](#)]
9. Sokkalingam, R.; Sivaprasad, K.; Muthupandi, V.; Prashanth, K.G. Dissimilar welding of Al<sub>0.1</sub>CoCrFeNi high-entropy alloy and AISI304 stainless steel. *J. Mater. Res.* **2019**, *35*, 2683–2694. [[CrossRef](#)]
10. Maity, T.; Prashanth, K.G.; Balci, O.; Wang, Z.; Jia, Y.D.; Eckert, J. Plastic deformation mechanisms in severely strained eutectic high entropy composites explained via strain rate sensitivity and activation volume. *Compos. Part. B: Eng.* **2018**, *150*, 7–13. [[CrossRef](#)]
11. Maity, T.; Prashanth, K.G.; Janda, A.; Kim, J.T.; Spieckermann, F.; Eckert, J. Mechanism of high-pressure torsion-induced shear banding and lamellar thickness saturation in Co-Cr-Fe-Ni-Nb high-entropy composites. *J. Mater. Res.* **2019**, *34*, 2672–2682. [[CrossRef](#)]
12. Gludovatz, B.; Hohenwarter, A.; Catoor, D.; Chang, E.H.; George, E.P.; Ritchie, R.O. A fracture-resistant high-entropy alloy for cryogenic applications. *Science* **2014**, *345*, 1153–1157. [[CrossRef](#)] [[PubMed](#)]
13. Zhang, Z.J.; Mao, M.M.; Wang, J.; Gludovatz, B.; Zhang, Z.; Mao, S.X.; George, E.P.; Yu, Q.; Ritchie, R.O. Nanoscale origins of the damage tolerance of the high-entropy alloy CrMnFeCoNi. *Nat. Commun.* **2015**, *6*, 10143. [[CrossRef](#)] [[PubMed](#)]
14. Maity, T.; Dutta, A.; Jana, P.P.; Prashanth, K.G.; Eckert, J.; Das, J. Influence of Nb on the microstructure and fracture toughness of (Zr<sub>0.76</sub>Fe<sub>0.24</sub>)<sub>100-x</sub>Nb<sub>x</sub> nano-eutectic composites. *Materials* **2018**, *11*, 113. [[CrossRef](#)] [[PubMed](#)]
15. Hemphill, M.A.; Yuan, T.; Wang, G.Y.; Yeh, J.W.; Tsai, C.W.; Chuang, A.; Liaw, P.K. Fatigue behavior of Al<sub>0.5</sub>CoCrCuFeNi high-entropy alloys. *Acta Mater.* **2012**, *60*, 5723–5734. [[CrossRef](#)]
16. Tsao, T.K.; Yeh, A.C.; Kuo, C.M.; Kakehi, K.; Murakami, H.; Yeh, J.W.; Jian, S.R. The High Temperature Tensile and Creep Behaviors of High Entropy Superalloy. *Sci. Rep.* **2017**, *7*, 12658. [[CrossRef](#)] [[PubMed](#)]
17. Liu, Y.X.; Cheng, C.Q.; Shang, J.L.; Wang, R.; Li, P.; Zha, J. Oxidation behavior of high-entropy alloys Al<sub>x</sub>CoCrFeNi (x = 0.15, 0.4) in supercritical water and comparison with HR3C steel. *Trans. Nonferr. Met. Soc.* **2015**, *25*, 1341–1351. [[CrossRef](#)]

18. Laplanche, G.; Volkert, U.F.; Eggeler, G.; George, E.P. Oxidation Behavior of the CrMnFeCoNi High-Entropy Alloy. *Oxid. Met.* **2016**, *85*, 629–645. [[CrossRef](#)]
19. Qiu, Y.; Thomas, S.; Gibson, M.A.; Fraser, H.L.; Birbilis, N. Corrosion of high entropy alloys. *Mater. Degrad.* **2017**, *1*, 15. [[CrossRef](#)]
20. Shi, Y.; Yang, B.; Liaw, P.K. Corrosion-Resistant High-Entropy Alloys: A Review. *Metals* **2017**, *7*, 43. [[CrossRef](#)]
21. Greer, A.L. Confusion by design. *Nature* **1993**, *366*, 303. [[CrossRef](#)]
22. Prashanth, K.G.; Scudino, S.; Murty, B.S.; Eckert, J. Crystallization kinetics and consolidation of mechanically alloyed Al<sub>70</sub>Y<sub>16</sub>Ni<sub>10</sub>Co<sub>4</sub> glassy powders. *J. Alloy. Compd.* **2009**, *477*, 171–177. [[CrossRef](#)]
23. Surreddi, K.B.; Scudino, S.; Sakaliyska, M.; Prashanth, K.G.; Sordelet, D.J.; Eckert, J. Crystallization behavior and consolidation of gas-atomized Al<sub>84</sub>Gd<sub>6</sub>Ni<sub>7</sub>Co<sub>3</sub> glassy powder. *J. Alloy. Compd.* **2010**, *491*, 137–142. [[CrossRef](#)]
24. Wang, Z.; Prashanth, K.G.; Scudino, S.; Chaubey, A.K.; Sordelet, D.J.; Zhang, W.W.; Li, Y.Y.; Eckert, J. Tensile properties of Al matrix composites reinforced with in situ devitrified Al<sub>84</sub>Gd<sub>6</sub>Ni<sub>7</sub>Co<sub>3</sub> glassy particles. *J. Alloy. Compd.* **2014**, *586*, S419–S422. [[CrossRef](#)]
25. Fu, X.; Schuh, C.A.; Olivetti, E.A. Materials selection considerations for high entropy alloys. *Scr. Mater.* **2017**, *138*, 145–150. [[CrossRef](#)]
26. Miracle, D.B.; Miller, J.D.; Senkov, O.N.; Woodward, C.; Uchic, M.D.; Tiley, J. Exploration and Development of High Entropy Alloys for Structural Applications. *Entropy* **2014**, *16*, 494–525. [[CrossRef](#)]
27. Sokkalingam, R.; Sivaprasad, R.; Muthupandi, V.; Duraiselvam, M. Characterization of Laser Beam Welded Al<sub>0.5</sub>CoCrFeNi High-Entropy Alloy. *Key. Eng. Mater.* **2018**, *775*, 448–453. [[CrossRef](#)]
28. Tan, Z.; Wang, L.; Xue, Y.; Zhang, P.; Cao, T.; Cheng, X. High-entropy alloy particle reinforced Al-based amorphous alloy composite with ultrahigh strength prepared by spark plasma sintering. *Mater. Des.* **2016**, *109*, 219–226. [[CrossRef](#)]
29. Velo, I.L.; Gotor, F.J.; Alcalá, M.D.; Real, C.; Córdoba, J.M. Fabrication and characterization of WC-HEA cemented carbide based on the CoCrFeNiMn high entropy alloy. *J. Alloy. Compd.* **2018**, *746*, 1–8. [[CrossRef](#)]
30. Zhou, S.; Liang, Z.J.; Zhu, Y.; Jian, R.; Wang, B.; Xue, Y.; Wang, L.; Wang, F. High entropy alloy: A promising matrix for high-performance tungsten heavy alloys. *J. Alloy. Compd.* **2019**, *777*, 1184–1190. [[CrossRef](#)]
31. German, R.M.; Bourguignon, L.L.; Rabin, B.H. Microstructure limitations of high tungsten content heavy alloys. *JOM* **1985**, *37*, 36–39. [[CrossRef](#)]
32. Satyanarayana, P.V.; Sokkalingam, R.; Sivaprasad, K.; Mukherjee, A.K. Effect of Composition on Tensile and Impact Properties of Tungsten-Based Heavy Alloy. *Mater. Sci. Forum* **2016**, *863*, 40–44. [[CrossRef](#)]
33. Bose, A.; Schuh, C.A.; Tobia, J.C.; Tuncer, N.; Mykulowycz, M.; Preston, A.; Barbati, A.C.; Kernan, B.; Gibson, M.A.; Krause, D.; et al. Traditional and additive manufacturing of a new Tungsten heavy alloy alternative. *Int. J. Refract. Met. Hard Mater.* **2018**, *73*, 22–28. [[CrossRef](#)]
34. Çalışkan, N.K.; Durlu, N.; Bor, Ş. Swaging of liquid phase sintered 90W-7Ni-3Fe tungsten heavy alloy. *Int. J. Refract. Met. Hard Mater.* **2013**, *36*, 260–264. [[CrossRef](#)]
35. Kiran, U.R.; Kumar, J.; Kumar, V.; Sankaranarayana, M.; Rao, G.V.S.N.; Nandy, T.K. Effect of cyclic heat treatment and swaging on mechanical properties of the tungsten heavy alloys. *Mater. Sci. Eng. A* **2016**, *656*, 256–265. [[CrossRef](#)]
36. Dinçer, O.; Pehlivanoglu, M.K.; Çalışkan, N.K.; Karakaya, I.; Kalkanli, A. Processing and microstructural characterization of liquid phase sintered tungsten–nickel–cobalt heavy alloys. *Int. J. Refract. Met. Hard Mater.* **2015**, *50*, 106–112. [[CrossRef](#)]
37. Das, J.; Kiran, U.R.; Chakraborty, A.; Prasad, N.E. Hardness and tensile properties of tungsten based heavy alloys prepared by liquid phase sintering technique. *Int. J. Refract. Met. Hard Mater.* **2009**, *27*, 577–583. [[CrossRef](#)]
38. Prabhu, G.; Kumar, N.A.; Sankaranarayana, M.; Nandy, T.K. Tensile and impact properties of microwave sintered tungsten heavy alloys. *Mater. Sci. Eng. A* **2014**, *607*, 63–70. [[CrossRef](#)]
39. Senthilnathan, N.; Annamalai, A.R.; Venkatachalam, G. Microstructure and mechanical properties of spark plasma sintered tungsten heavy alloys. *Mater. Sci. Eng. A* **2018**, *710*, 66–73. [[CrossRef](#)]
40. Li, Z.; Zhao, S.; Ritchie, R.O.; Meyers, M.A. Mechanical properties of high-entropy alloys with emphasis on face-centered cubic alloys. *Prog. Mater. Sci.* **2019**, *102*, 296–345. [[CrossRef](#)]
41. Schwab, H.; Prashanth, K.G.; Loeber, L.; Kuehn, U.; Eckert, J. Selective laser melting of Ti-45Nb alloy. *Metals* **2015**, *5*, 686–694. [[CrossRef](#)]

42. Mane, R.B.; Rajkumar, Y.; Panigrahi, B.B. Sintering mechanism of CoCrFeMnNi high-entropy alloy powders. *Powder Metall.* **2018**, *61*, 131–138. [[CrossRef](#)]
43. Praveen, S.; Murty, B.S.; Kottada, R.S. Alloying behavior in multi-component AlCoCrCuFe and NiCoCrCuFe high-entropy alloys. *Mater. Sci. Eng. A* **2012**, *534*, 83–89. [[CrossRef](#)]
44. Tsai, M.H.; Chang, K.C.; Li, J.H.; Tsai, R.C.; Cheng, A.H. A second criterion for sigma phase formation in high-entropy alloys. *Mater. Res. Lett.* **2016**, *4*, 90–95. [[CrossRef](#)]
45. Ji, W.; Wang, W.; Wang, H.; Zhang, J.; Wang, Y.; Zhang, F.; Fu, Z. Alloying behavior and novel properties of CoCrFeNiMn high-entropy alloy fabricated by mechanical alloying and spark plasma sintering. *Intermetallics* **2015**, *56*, 24–27. [[CrossRef](#)]
46. Moravcik, I.; Cizek, J.; Gouvea, L.; Cupera, J.; Guban, I.; Dlouhy, I. Nitrogen Interstitial Alloying of CoCrFeMnNi High Entropy Alloy through Reactive Powder Milling. *Entropy* **2019**, *21*, 363. [[CrossRef](#)]
47. Moravcik, I.; Gouvea, L.; Hornik, V.; Kovacova, Z.; Kitzmantel, M.; Neubauer, E.; Dlouhy, I. Synergic strengthening by oxide and coherent precipitate dispersions in high-entropy alloy prepared by powder metallurgy. *Scr. Mater.* **2018**, *157*, 24–29. [[CrossRef](#)]
48. Kumar, D.; Maulik, O.; Kumar, S.; Prasad, Y.V.S.S.; Kumar, V. Phase and thermal study of equiatomic AlCuCrFeMnW high entropy alloy processed via spark plasma sintering. *Mater. Chem. Phys.* **2018**, *210*, 71–77. [[CrossRef](#)]
49. Takeuchi, A.; Inoue, A. Calculations of Mixing Enthalpy and Mismatch Entropy for Ternary Amorphous Alloys. *Mater. Trans. JIM* **2000**, *41*, 1372–1378. [[CrossRef](#)]
50. Mondal, A.; Upadhyaya, A.; Agrawal, D. Effect of heating mode on sintering of tungsten. *Int. J. Refract. Met. Hard Mater.* **2010**, *28*, 597–600. [[CrossRef](#)]
51. German, R.M.; Bose, A.; Mani, S.S. Sintering time and atmosphere influences on the microstructure and mechanical properties of tungsten heavy alloys. *Metall. Trans. A* **1992**, *23*, 211–219. [[CrossRef](#)]
52. Li, Y.; Hu, K.; Li, X.; Ai, X.; Qu, S. Fine-grained 93W–5.6Ni–1.4Fe heavy alloys with enhanced performance prepared by spark plasma sintering. *Mater. Sci. Eng. A* **2013**, *573*, 245–252. [[CrossRef](#)]



© 2019 by the authors. Licensee MDPI, Basel, Switzerland. This article is an open access article distributed under the terms and conditions of the Creative Commons Attribution (CC BY) license (<http://creativecommons.org/licenses/by/4.0/>).